Molecular dynamics simulation of thermal transport in semicrystalline polyethylene: Roles of strain and the crystalline-amorphous interphase region

Cite as: J. Appl. Phys. **130**, 225101 (2021); https://doi.org/10.1063/5.0067999 Submitted: 21 August 2021 • Accepted: 18 November 2021 • Published Online: 08 December 2021

Jixiong He and 🔟 Jun Liu

COLLECTIONS

Paper published as part of the special topic on Engineering and Understanding of Thermal Conduction in Materials







ARTICLES YOU MAY BE INTERESTED IN

Momentum(k)-space carrier separation using SiGeSn alloys for photodetector applications Journal of Applied Physics 130, 223102 (2021); https://doi.org/10.1063/5.0063179

Study on pore size distribution and thermal conductivity of aramid nanofiber aerogels based on fractal theory

Journal of Applied Physics 130, 225104 (2021); https://doi.org/10.1063/5.0068459

From nanowires to super heat conductors

Journal of Applied Physics 130, 220901 (2021); https://doi.org/10.1063/5.0069551





Molecular dynamics simulation of thermal transport in semicrystalline polyethylene: Roles of strain and the crystalline-amorphous interphase region

Cite as: J. Appl. Phys. **130**, 225101 (2021); doi: 10.1063/5.0067999 Submitted: 21 August 2021 · Accepted: 18 November 2021 · Published Online: 8 December 2021







Jixiong He¹ and Jun Liu^{1,2,a)}

AFFILIATIONS

¹Department of Mechanical and Aerospace Engineering, North Carolina State University, Raleigh, North Carolina 27695, USA ²Organic and Carbon Electronics Lab (ORaCEL), North Carolina State University, Raleigh, North Carolina 27695, USA

Note: This paper is part of the Special Topic on Engineering and Understanding of Thermal Conduction in Materials.

a)Author to whom correspondence should be addressed: jliu38@ncsu.edu

ABSTRACT

With potential thermal management applications, such as plastic heat exchangers and thermal interface materials, thermally conductive polymers have gained renewed interest in the past decade. Ultradrawn polyethylene fibers and films have been experimentally shown to have thermal conductivities at least two orders of magnitude of these in their amorphous counterparts. However, the theoretical molecular-level understanding of strain effects on the thermal transport in drawn semicrystalline polymers, such as polyethylene, especially the roles of different interlamellar chain topologies in the crystalline-amorphous interphase region, remains elusive. Using molecular dynamics simulations, we investigated the strain effects on the thermal conductivity and vibrational transport in a simplified sandwich semicrystalline structure. We found that the topology of the interlamellar chains determines the dependence of thermal conductivity on strains. Comparing thermal resistances at different regions in the interlamellar structure, thermal resistance at the amorphous region is not necessarily the highest; the interphase region with the transition from the crystalline to amorphous state can have a much higher resistance. We conducted the frequency domain analysis to obtain the heat flux spectrum in the crystalline-amorphous interphase region and found that the vibrational modes at intermediate and high frequencies can contribute more than these at relatively low frequencies to the total heat flux because of the complex interlamellar chain topologies (e.g., loop chains). Our work provides molecular-level understandings of the structural-property relationship in semicrystalline polymers with strains, which could assist the design and development of thermally conductive polymers for thermal management applications.

Published under an exclusive license by AIP Publishing. https://doi.org/10.1063/5.0067999

I. INTRODUCTION

It is desirable to achieve high thermal conductivity in polymers for thermal management in applications¹ such as electronics packaging,² thermal interface material,³ solar cell,⁴ battery,⁵ and plastic heat exchanger.⁶ These potential applications have motivated researchers to explore thermally conductive polymers using a variety of fabrication methods, such as mechanical stretching,^{7,8} electrospinning,⁹ nanoscale templating,¹⁰ blending,¹¹ and compositing,¹² and employing molecular-level engineering approaches.^{13,14} When polymers are stretched, polymer chains are highly aligned and the chain entanglements are significantly reduced, which can

lead to a thermal conductivity increase by two to three orders of magnitude. $^{15-17}$ For example, the room-temperature thermal conductivity of amorphous polyethylene (PE) is 0.2 W/(m K). In contrast, the thermal conductivity of the commercial ultra-drawn single PE microfibers (e.g., spectra 2000) has been measured as $\sim 10-16 \text{ W/(m K)}$. 18 Zhu *et al.* showed that the thermal conductivity of those commercial microfibers could further increase $\sim 80\%-150\%$ with a moderate draw ratio of 2–6 under heating. 19 Ultra-drawn PE nanofibers were reported to have as high room-temperature thermal conductivity as $\sim 50-100 \text{ W/(m K)}$. 7,20 Besides stretched fibers, PE films fabricated by roll-to-roll stretching can

achieve a high room-temperature thermal conductivity, \sim 60 W/(m K). In all these nanofiber, microfiber, and film samples, the PE is in a semicrystalline state with high structural anisotropy due to stretching.

The semicrystalline polymer is a two-phase mixture system with the ordered crystalline lamellar phase and the disordered amorphous phase. A simplified repeating unit of drawn semicrystalline polymers is a sandwich structure with two crystalline regions at the sides called lamella and the amorphous region in the middle called the interlamellar region. ^{21,22} The study of the structure-property relationship in drawn semicrystalline polymers dates back to the early 1950s. Theoretically, the series model is widely used to apply the thermal resistance network concept in such a two-phase mixture system where the bulk thermal conductivity values of the corresponding crystalline and amorphous polymers are used.²³ For example, in the analysis of the experimental data in the work by Zhu et al., 19 the thermal conductivity of crystalline and amorphous regions was taken from the measurement results in nanofibers, which is very close to the bulk values. However, our previous simulation work on unstretched PE models shows that the series model underestimates the thermal conductivity of semicrystalline polymers at high crystallinity due to the ignorance of the important role of chain topologies in the interlamellar region, especially the bridge chains connecting two adjacent crystalline lamel-Similar bridging effects are also found in other material systems. 12,25-27 To incorporate the bridge chains in the model, Takayanagi proposed a model that specifically treats bridge chains the same as the crystalline stems, which are aligned in the extrusion direction and have the same thermal conductivity as in the crystalline stems. 28 Similar to Takayanagi's model, the HalpinTsai equation 29 and Cox model 30 have been proposed to treat bridges as straight ultra-aligned chains. We notice that in the model analysis of high thermal conductivity in ultra-drawn PE films by Xu et al.,8 the thermal conductivity of the amorphous region in the stretched semicrystalline films deviates significantly from the bulk amorphous and the ideal crystal values. It increases initially with the draw ratio up to 10, stays at a plateau at the draw ratio 10-60, and then strongly increases with the draw ratio up to 110. Inspired by this result, we expect a substantial role of interlamellar chain topologies in the strained semicrystalline polymers, which will not always lead to a constantly high thermal conductivity value in this region as in the lamellas.

The increase in thermal conductivity in semicrystalline polymer fibers or films with strains is related to the change in their chain structure.^{8,31} Many classical studies a few decades ago revealed the microstructure and molecular-level structure change in drawn semicrystalline polymers.^{31–34} There are two stages of structural change upon mechanical stretching after the transformation from a spherulitic structure into a bundle-of-microfibrils structure, which are crucial in understanding the strain effects on thermal conductivity: (1) With relatively small strains, the crystalline lamellae will shatter into several smaller crystalline regions sandwiched by some amorphous regions. The intrafibrillar bridge chains will connect the crystalline regions. (2) With relatively large strains, these intrafibrillar chains and chains outside the microfibrils region will extend and align themselves. In the past decade, there are also many molecular-level simulation studies to understand the

structural evolution and chain dynamics during the stretching of semicrystalline polymers. For example, atomistic simulations from Rutledge *et al.*^{22,35–39} have provided substantial insights into the plastic deformation in semicrystalline PE on the roles of interphase topology, entanglements, and chain dynamics, starting from the bundle-of-microfibrils-like structure. However, a similar molecular-level simulation is missing for the thermal transport analysis, which is necessary to correlate the chain structure and the thermal transport properties during the stretching process and build better models for the processing-structure-thermal conductivity relationship in drawn semicrystalline polymers.

In this work, we studied the strain effects on thermal transport in semicrystalline PEs using molecular dynamics (MD) simulations, with a focus on the roles of interlamellar chain topology and the crystalline-amorphous interphase region. This study is based on our previous studies where we simulated the thermal transport in semicrystalline PEs without strains²⁴ and explored strain effects in crystalline PEs¹⁷ and polymer fibers.⁴⁰ Here, we built four most representative repeating units of semicrystalline PE systems with different crystallinities and interlamellar topology using the enhanced Monte Carlo (EMC) method³⁵ and stretched them. This repeating unit is the same as used in the studies of Rutledge et al.. The dependence of their thermal conductivities on mechanical strains was calculated by the nonequilibrium molecular dynamics (NEMD) simulations. We focus on small and intermediate strains in this work where the sandwich structure is still valid and the intrafibrillar chains do not break. We found that the interlamellar chain topologies between the two crystalline lamellas determine the strain effects on thermal conductivity. In addition, we applied the frequency direct decomposed method⁴¹ (FDDDM) to analyze the vibrational transport across the crystalline-amorphous interphase region and found that vibrational modes with intermediate and high frequencies contribute more than 50% to the total heat flux due to the complex interlamellar chain topologies.

II. MODELS AND METHODS

A. Semicrystalline polyethylene model construction

Figure 1 illustrates a simplified model of a stretched semicrystalline polymer fiber or a film. The crystallite (i.e., crystalline lamellae or crystalline stem) will be aligned in the stretched direction and interlamellar chains connect crystallites, which mimics the bundle-of-microfibrils-like structure. A typical repeating unit consists of two crystalline regions and an interlamellar region. We considered three types of chain topologies in the interlamellar region, i.e., bridges, loops, and tails. Among these, a bridge is defined as the segments connecting the crystalline stems throughout the interlamellar region; a loop connects crystalline stems at the same side; and for a tail, one side of it is connected to the crystalline stems while the other side terminates.

We focus on the semicrystalline PE for simplicity in its chemical structure. We used the unit cell of the PE crystal to represent the crystalline region in the semicrystalline PE, which is a different but simplified version from the switchboard model of a polymer crystalline lamella. We employed the same method as in our previous work, ²⁴ i.e., the EMC method, ^{35–37} to build the semicrystalline PE models. Here we only describe the major procedures with more

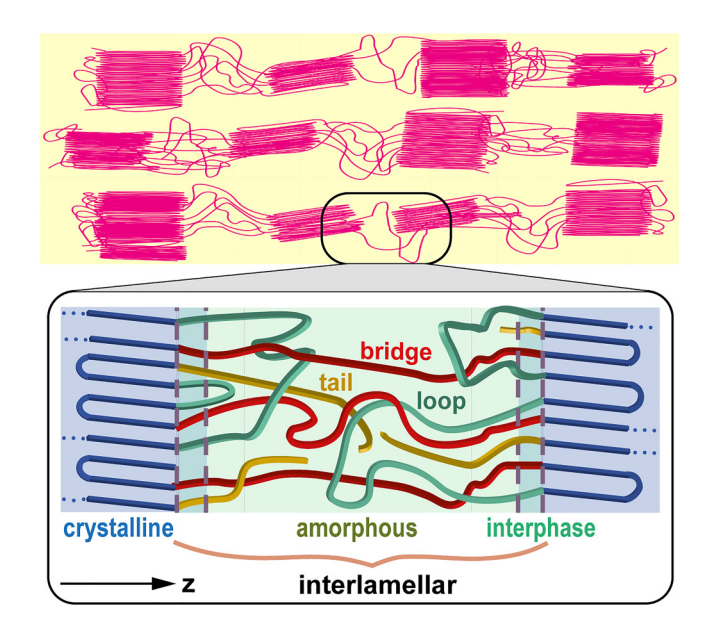
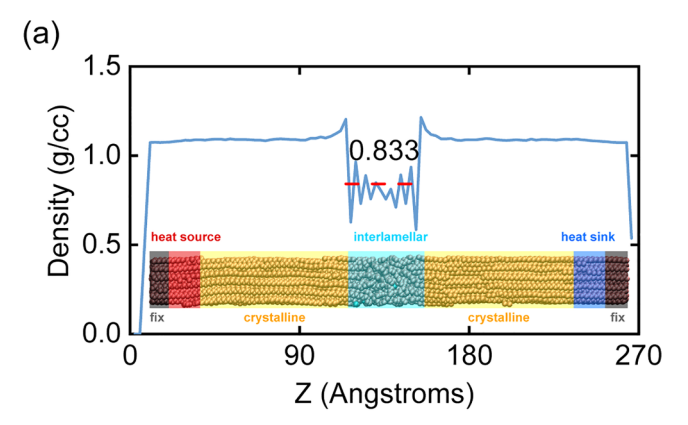


FIG. 1. Schematic diagram of the representative repeating unit of a stretched polymer fiber or a film. The bottom panel of the zoomed-in view shows a representative unit of the semicrystalline structure, which contains two crystalline regions on both sides (blue shaded regions), two interphase regions (green shaded regions), and an amorphous region (intermediate light green region). The interphase regions and the amorphous region sandwiched in the middle are defined as the interlamellar region. These regions are distinguished according to the density profiles. Different types of chains in the interlamellar regions are illustrated using different colors: Bridges are denoted by red lines, loops are denoted by green lines, and tails are denoted by yellow lines.

details referred to our previous publication. (1) First, a crystalline PE structure comprising $3 \times 5 \times 100$ unit cells was generated with the lattice constant a = 7.7175 Å, b = 4.45 Å, c = 2.527 Å, resulting in 6000 atoms and 30 chains in the simulation box. The united-atom force field was used to describe the interatomic potential.²⁴ The chains were then aligned parallel to the z-direction of the simulation box. To create different effective crystallinity X in the simulation domain, we selected and fixed 18 and 28 layers of atoms (each layer contains $3 \times 5 \times 1$ unit cells) on each side in the z-direction as the crystalline region for the X = 51% and X = 80%effective crystallinity configurations, respectively. The effective crystallinity X is defined as the ratio between the effective lengths of crystalline and the whole semicrystalline regions. Periodic boundary conditions are applied in all directions. (2) Next, 5 or 10 of the 30 chains were cut randomly, and 325 or 130 united atoms in these chains were removed in X = 51% and 80% configurations, respectively, to match the experimental amorphous density of ~0.855 g/cc at 300 K and 1 atm. 42 (3) Then, all the united atoms in the interlamellar region underwent random Monte Carlo moves, including single-site displacement, end-rotation, re-bridging, end-reptation, and end-bridging, to form the interphase and amorphous regions. Among these moves, bond formation and breakage were involved. During this procedure, the number of tails $(N_T = 10)$ and the total number of bridges and loops $(N_B + N_L = 25)$ remained the same.

These random Monte Carlo moves were performed at 10 000 K to promote rapid randomization of the interlamellar configuration, generating the amorphous phase. (4) Finally, these configurations were equilibrated at 10 000 K for 20 000 Monte Carlo cycles, followed by quenching from 10 000 to 300 K stepwise during 600 000 cycles. The quenching was performed in the sequence of 5000, 2000, 1000, 750, 500, 400, 350, and 300 K in 20 000, 40 000, 40 000, 40 000, 60 000, 80 000, 160 000, and 160 000 cycles, respectively. An advantage in building configurations by the EMC method is that the atoms in the interphase region are covalently bonded to the crystalline stems and amorphous regions instead of simply stacked through the van der Waals interactions. After quenching, the interlamellar region evolves into an amorphous region and a transitional interphase region.

Figure 2 shows the configurations of semicrystalline PE with X=80% and X=51% built by the EMC method. The density profiles are also shown so that the regions of crystalline, interphase, and amorphous can be distinguished. The average density of the crystalline region is $\sim 1 \, \text{g/cc}$ and that of the amorphous region is



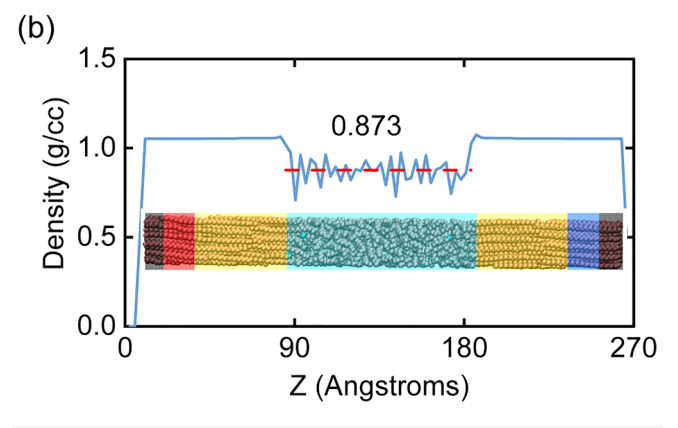


FIG. 2. Schematic diagram for the semicrystalline PE models with (a) 80% and (b) 51% crystallinity. Atoms in crystalline and interlamellar regions are marked in yellow and blue, respectively. The density profile (density as a function of Z) is plotted. For the NEMD simulation, vacuum regions are added on each end along the z-direction. Atoms in the boundary regions are fixed. Heat source and sink are applied in the regions adjacent to the fixed regions.

 \sim 0.87 and \sim 0.83 g/cc, which is comparable with the experimental results, 0.85 g/cc. The drop in the density from crystalline to amorphous regions occurs in a transition region, which is defined as the interphase region. The thickness of the interphase region is estimated as \sim 1 nm.

Table I summarizes the four models investigated in this work. The models M1, M2, and M3 are built at the same crystallinity, X = 51%, with an increasing number of bridge chains. The model M4 is built with a much higher crystallinity, X = 80%, with a substantially increased number of bridges. The goal is to compare the thermal conductivity and the thermal transport process in both unstretched and stretched models.

B. Molecular dynamics simulation and thermal conductivity calculation

MD simulations were performed to equilibrate the ensembles generated by the EMC methodology and to study their thermal properties using the LAMMPS package. 43 The timestep was 1 fs in all simulations because the united atom model rather than the all-atom model was used so that there are no fast-vibrating hydrogens in our model. The same united-atom force field as in the EMC method was used here. Periodic boundary conditions were applied in all three directions. Independent configurations for each crystallinity were equilibrated in the NPT (constant total number of particles N, pressure P, and temperature T) ensemble for 8 ns, during which the pressure is 1 atm and temperature is 300 K. The pressure and temperature damping parameters were 1000 and 100 fs, respectively. Then, 0.2 ns NVE ensemble (constant total number of particles N, the volume V, and the total energy E of the system) was performed for relaxation. During MD simulations, the numbers of bridges, loops, and tails do not change.

The thermal conductivity calculation was done by the NEMD simulation method. ^{15,16,20,24,25} Figure 2(a) shows the simulation setup. To establish a temperature gradient along the z-direction without introducing coupling between thermostats, vacuum regions with a size larger than the cut-off distance for the united-atom force field were added on each end and a certain number of layers on both ends were fixed. The heat source and heat sink regions were controlled by the Langevin thermostat, and the temperature of the region was set to 350 and 250 K, respectively.

The non-equilibrium simulations were performed for 5 ns to make sure that the system has reached a steady state. In the steady

TABLE I. Parameters in each semicrystalline PE model configuration investigated in this work. The models M1, M2, and M3 have the same crystallinity. The model M4 has a higher crystallinity. The bridge, tail, and loop numbers of each model are listed.

Model	Crystallinity, X (%)	Bridge number, N_B	$\begin{array}{c} \text{Tail} \\ \text{number, } N_T \end{array}$	$\begin{array}{c} \text{Loop} \\ \text{number, } N_L \end{array}$
M1	51	1	10	24
M2	51	2	10	23
M3	51	3	10	22
M4	80	7	10	18

state, the heat flux along the z-direction is

$$q_z = \frac{1}{2A} \left(\left| \frac{\Delta E_{source}}{\Delta t} \right| + \left| \frac{\Delta E_{sink}}{\Delta t} \right| \right). \tag{1}$$

A is the cross-sectional area in the x-y plane; Δt is the timestep; and ΔE_{source} and ΔE_{sinik} are the amount of heat added to the heat source and subtracted from the heat sink, respectively, which can be recorded during the simulation. The effective thermal conductivity of the interlamellar region Δ_e is defined as

$$q_z = \Lambda_e \frac{\Delta T}{\Delta L},\tag{2}$$

where ΔL is the length of the interlamellar region and ΔT is the temperature difference across this region. All the parameters were calculated in the z-direction. To obtain accurate ΔT , the temperature profile of semi-crystalline PE was averaged over the last 1 ns in the NVE ensemble.

C. Stretching semicrystalline polyethylene

We used the engineering strain ϵ to describe the stretching process, $\varepsilon = L_t/L_0 - 1$, where L_t and L_0 are the final length and initial length. We used the "fix deform" command in LAMMPS and changed the dimension of the simulation box at a constant engineering strain rate. The engineering strain rate in this work is $5 \times 10^7 \, \mathrm{s}^{-1}$, which is comparable to the previous work by Kim *et al.*³⁶ All the models were stretched with an engineering strain ε from 0 to 0.3 in a uniaxial extension fashion and the configuration models at $\varepsilon = 0$, 0.15, and 0.3 were recorded for further analysis. The models will then be relaxed in the NVE and NVT ensembles. More details can be found in our previous publication. We note that during the stretching process of some models, a portion of loops and tails can temporarily act as bridges connecting crystalline parts on two sides. After relaxing these structures in NVE and NVT ensembles, some loops and tails will shrink back to the crystalline side, whereas others remain connecting.

III. RESULTS AND DISCUSSION

A. Strain effect on the chains in the interlamellar region

We have shown in our previous work²⁴ that the contribution to the thermal transport in the interlamellar region from tail and loop chains is not negligible at the intermediate crystallinity, especially when the number of bridge chains is small. When the semicrystalline PE with the intermediate crystallinity is stretched, it remains unknown how the tails, loops, and bridges contribute to the thermal transport. Moreover, multiple configurations exist for the interlamellar chain topologies even when the initial crystallinity is the same. In this section, we first examine the interlamellar chain topologies when the semicrystalline PE is stretched. Figure 3 shows the snapshots of three semicrystalline PE models under strains at the same crystallinity X = 51%. The three chain topologies in the interlamellar region, i.e., tails, loops, and bridges, can entangle with each other in the unstretched model. When strains are applied,

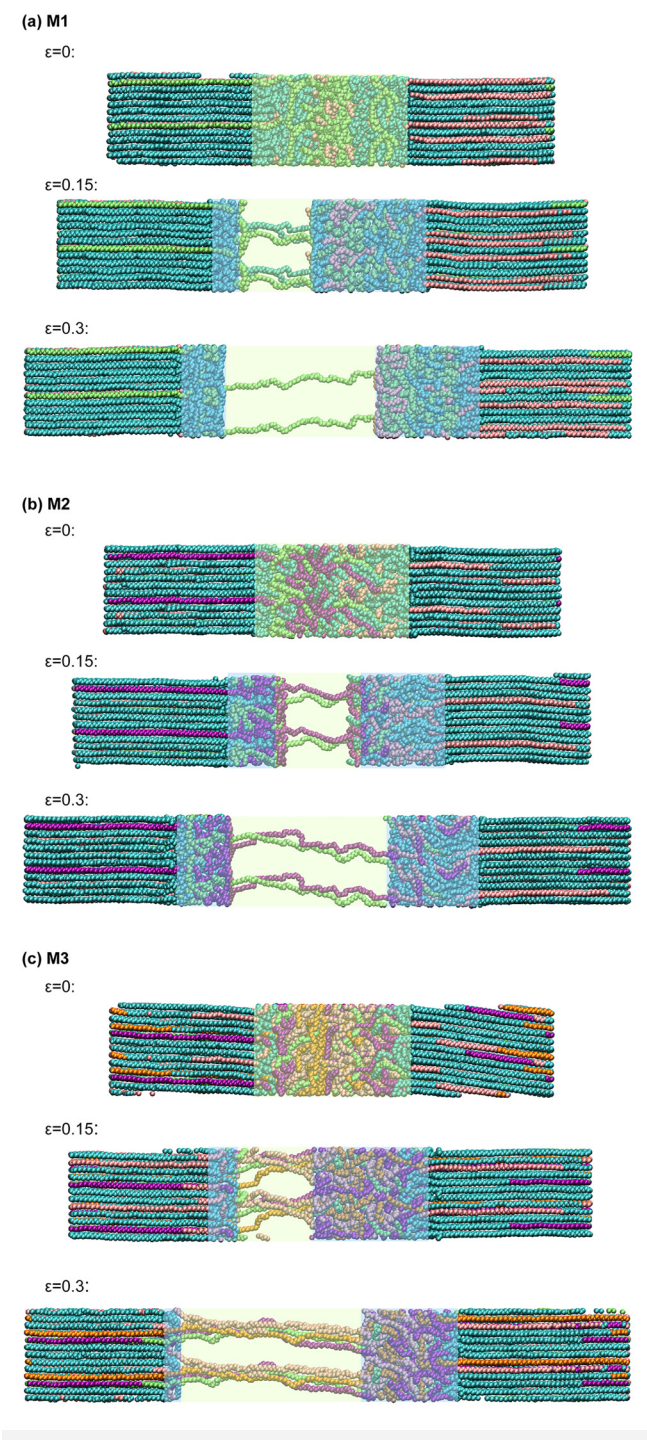


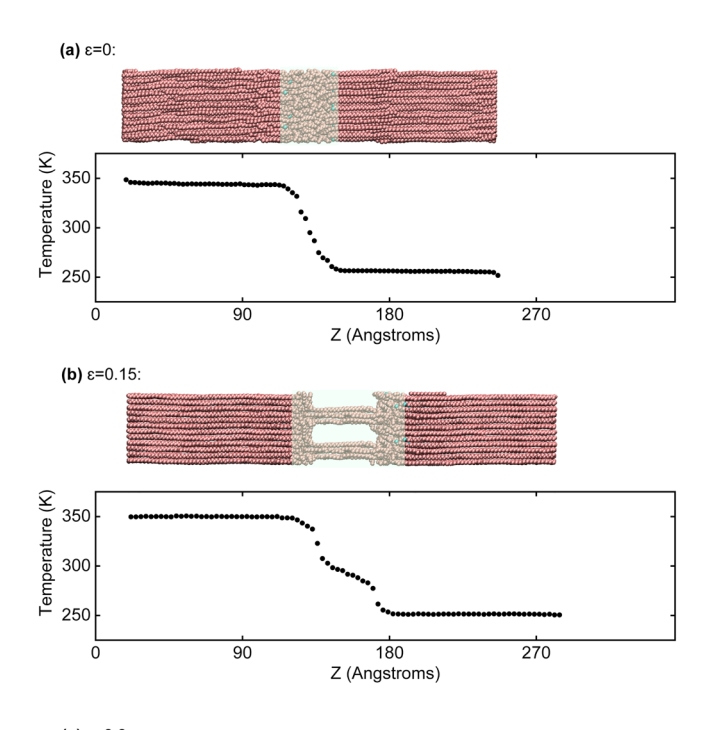
FIG. 3. Snapshots of semicrystalline PE models (a) M1, (b) M2, and (c) M3 under stretching with engineering strains ε = 0, 0.15, and 0.3. For better visualization, the model is repeated once in the vertical direction in these snapshots, and the interlamellar region is masked. Colors represent different topologies of chains: blue for loop chains, pink for tail chains, green for the first bridge chain, purple for the second bridge chain, and orange for the third bridge chain.

these entanglements could retain or disappear. Figure 3(a) illustrates the model M1 where a loop chain connects the two interphase regions, functioning as a "bridge" chain, at $\varepsilon = 0.15$. The loop chain eventually unhooks and shrinks back to one side at $\varepsilon = 0.3$, leaving only one bridge chain in the middle. Figure 3(b) shows the model M2 where only two bridges directly connect the two crystalline stems. The chains are more coiled at a smaller strain $\varepsilon = 0.15$ and become more aligned at a larger strain $\varepsilon = 0.3$. Figure 3(c) shows the model M3 where three bridges and one tail connect the two crystalline stems at $\varepsilon = 0.15$ and this topological configuration does not change even at $\varepsilon = 0.3$. At $\varepsilon = 0.3$, the chains are stretched and less coiled, but the tail chain remains to entangle with the other three bridge chains. Here the tail chain functions as if it was a bridge chain, but the difference between the tail chain and a bridge chain is that the tail chain is not covalently bonded to the other side. Figure 4 shows the snapshots of model M4 with the crystallinity X = 80%. Due to the higher crystallinity and the larger number of bridge chains compared to models M1-M3, the bridge chains tend to easily align with the stretching direction. At $\varepsilon = 0.15$ and $\varepsilon = 0.3$, the loop and tail chains rest at the interphase region with only local entanglements with bridge chains. This observation is in distinct contrast with the models M1 and M3 under stretching where the tail or loop chains can reach further into the opposite interphase region and entangle with the bridge chains.

One common feature in the chain configurations with our strained models is the formation of cavitation, i.e., longitudinal void, in the amorphous region. This configuration is consistent with the schematics shown in Fig. 1 and also schematics shown in the work of both Xu et al. and Zhu et al. 8,19 To understand how the interlamellar topology affects the thermal transport in strained semicrystalline polymers and also conduct the phonon transport analysis later, we need to have a minimum change of the crystalline lamellar regions and the deformation is only localized in the interlamellar and non-crystalline regions. Similar treatments have been used in building thermal conductivity models for semicrystalline polymers, such as in Choy's model and Takayanagi's model. In MD simulations, whether the cavitation will form or not during the stretching process is determined by the strain rate and the simulation temperature. Yeh et al., 37 Ranganathan et al., 39 and Kim et al.³⁶ have shown that in the tensile drawing of semicrystalline polymers, there is a competition between cavitation and activation of crystal plasticity. They have found that when the strain rate is higher $(5 \times 10^7 \, \text{s}^{-1})$, the same as in our simulation) at a simulation temperature of 350 K, the cavity will form. When the strain rate is an order of magnitude smaller, the melting and re-crystallization will be observed during the simulation of a onedimensional semicrystalline unit. However, when the temperature is much lower (e.g., 250 K), the liquid-like response required for melting and re-crystallization events is suppressed; only the cavitation will be observed in the simulation.

B. Strain effect on the thermal transport in the interlamellar region

The thermal transport in the interlamellar region in each model was investigated by the NEMD simulation. After the



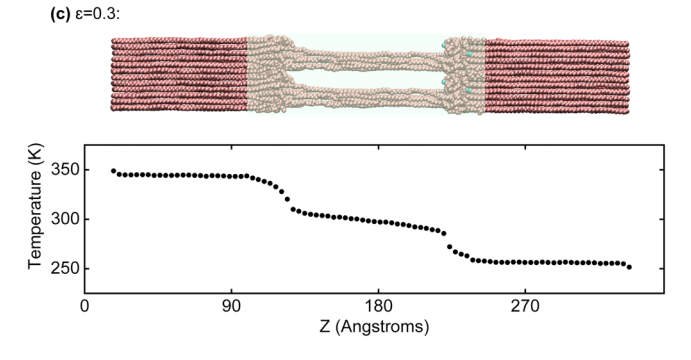


FIG. 4. The snapshots of the semicrystalline PE model M4 under stretching with engineering strains (a) ϵ = 0, (b) ϵ = 0.15, and (c) ϵ = 0.3. For better visualization, the model is repeated once in the vertical direction in these snapshots. The interlamellar region is masked. The temperature profiles obtained from NEMD simulations are also shown for each model. The location Z is matched with the snapshot.

molecular system reached a steady state, the temperature profile, which is the average temperature as a function of the location Z, was plotted. Figure 4 shows three temperature profile examples in model M4 with different strains. The heat current flows from the left crystalline stem, through the interphase region, across the interface between the interphase region and the amorphous region, along the chains in the amorphous region, across the other interface and interphase region, and finally reaches the right crystalline stem. Even though the amount of total heat current Q flowing across the cross-sectional area A is the same at different locations or regions, the relative temperature drops across each region are

TABLE II. Thermal transport properties of semicrystalline PE models at three different strains. The model index represents the model number and strain value. For example, the index M1_15 refers to model M1 at a strain of 0.15. Δ T1, Δ T2, and Δ T3 refer to the temperature drop at the interphase region, across the interface between the interphase and the amorphous region, respectively. Here the "amorphous" is loosely defined in the strained models, where there might be only a few bridge chains in this region. Q is the heat current flowing in the interlamellar region and the amorphous region, respectively.

Model	ΔT_1 (K)	ΔT ₂ (K)	ΔT ₃ (K)	Q (nW)	$\Lambda_{\rm e}$ [W/(mK)]	Λ_a [W/(mK)]
M1 0	6.1	N/A	91.3	6.3	0.11	0.10
M1_15	58.4	26.4	13.7	3.5	0.08	0.13
M1_30	28.6	35.2	35.4	1.7	0.05	0.07
M2_0	6.7	N/A	90.2	8.2	0.14	0.13
M2_15	35.5	46.4	16.7	3.9	0.10	0.09
M2_30	29.7	36.7	31.8	3.4	0.11	0.15
M3_0	9.3	N/A	87.2	9.3	0.15	0.14
M3_15	56.6	27.9	12.7	6.9	0.16	0.30
M3_30	53.7	15.8	27	6.5	0.20	0.38
M4_0	17.6	N/A	64.7	42.2	0.27	0.20
M4_15	25.5	50.1	8.4	50.7	0.97	3.69
M4_30	38	23.7	24.3	55.8	1.80	3.85

substantially different. A comparison among the magnitudes of temperature drop across different regions ΔT indicates the distribution of the thermal resistances R in the interlamellar region of the same PE model because $R = A\Delta T/Q$. Table II shows a more detailed comparison among the temperature drops at three regions in the interlamellar region. For the unstretched model, separating the interface region from the interphase region is not necessary (marked N/A in the Table). For the stretched model, the interface between the interphase and the amorphous region creates a notable temperature drop, as shown in Figs. 4(b) and 4(c). Even though the "amorphous" region only has a few bridges left with stretching, we still adopt the same name for this region here.

We will first compare the relative thermal resistance contributions from different parts of the interlamellar region. For a certain model (e.g., M1_15), the heat flow and cross-sectional area are the same for different regions, so the temperature drops at different regions ($\Delta T1$, $\Delta T2$, and $\Delta T3$) represent the thermal resistances. When the semicrystalline PE models are not stretched, e.g., M1_0, M2_0, and M3_0, the thermal resistance contribution from the amorphous region dominates (>90% contribution), which results from the low thermal conductivity of randomly oriented polymer chains in this region. The interphase region, which is the transition from the crystalline region with atomic order to the amorphous region that lacks long-range order, also adds a small but nonnegligible (6%-10%) contribution to the total thermal resistance. When the semicrystalline PE models are stretched, three regions generate thermal resistance: the interphase region, the amorphous region, and the interface between these two regions. Here we describe the observations in Table II based on the comparisons among M1-M3 with the same crystallinity: (1) The interphase region significantly contributes to the total thermal resistance (30%-60%)

because this region was originally the amorphous region before stretched, filled with random orientation of chains. When the same polymer is stretched from $\varepsilon = 0.15$ to 0.3, the relative contribution to the total thermal resistance decreases but the absolute thermal resistance almost remains the same (the difference is less than 4%). (2) The amorphous region increases its relative contribution to the total thermal resistance with increasing strain from $\varepsilon = 0.15$ to 0.3. For M1, the number of chains connecting the two crystalline stems reduces from one bridge chain and one loop chain to only one bridge chain. Therefore, thermal resistance of this region substantially increases due to fewer channels for thermal transport and the increased volume of voids between chains. The voids will not carry any vibrational energy so that the thermal energy travels solely via the chains connecting the stems. For M2 and M3, the chains connecting the stems become more aligned with strains that make the thermal resistance along the chains reduced, but the thermal resistance of this region still increases due to the increased volume of voids. (3) The interface region decreases its relative contribution to the total thermal resistance with increasing strain from $\varepsilon = 0.15$ to 0.3 for M2 and M3 but shows an opposite trend for M1. Even though the thickness of the interface region is much smaller than the other two regions, the thermal resistance is non-negligible. Likely, the partial transmission of incident vibrational modes, the conversion between modes, and the anharmonic scatterings among modes cause a temperature drop and then a thermal resistance at the interface between the interphase and amorphous regions. 44-47 When the semicrystalline PE is stretched with only a few connecting chains in the amorphous region, these connecting chains (e.g., bridges) become the only channels for vibrational energy to transport, so the interface resistance is determined by the chains in the amorphous region to some extent. For M1, the number of connecting chains decreases from two to one, which explains the increase in the relative contribution of interface resistance. To quantify this change, the interfacial thermal resistance in the model M_15 is 7.5 K/nW, whereas it is 20.7 K/nW in M1_30, an increase of ~2.8 times. For M2 and M3, this relative contribution decreases due to the better alignment of bridge chains with strains.

Now we compare the relative thermal resistance contributions from different parts of the interlamellar region for model M4, with a direct comparison of the temperature profiles at different strains in Fig. 4 and the relative contributions in Table II. The contribution from the interphase region to the total thermal resistance is larger than 20%, and this contribution increases with larger strains. Comparing the resistances at $\varepsilon = 0.15$ and 0.3, the largest thermal resistance is not from the amorphous region with multiple bridge chains. These short and aligned bridge chains effectively transport vibrational energy from one side to the other side. The consequence of the thermally conductive bridge chains is the relatively large resistance at the interface and interphase regions, which can be seen from the temperature drops at these two regions. The dominant thermal resistance shifts from the interface region to the interphase region from $\varepsilon = 0.15$ to $\varepsilon = 0.3$ due to the decreasing resistance from the interface region, which arises from the enhanced capability to transport heat on the bridge chains with much better chain alignments.

We then compare the thermal conductivity in the amorphous region Λ_a and the effective thermal conductivity of the entire interlamellar region Λ_e in Table II. At zero strain, Λ_e almost equals Λ_a , which

is expected. Even though there are certain resistances at the interphase regions, they are much smaller than those at the amorphous regions. For models M1 and M2 at strains $\epsilon=0.15$ and 0.3, Λ_e is about 60%–75% lower than Λ_a due to the large thermal resistances at both the amorphous region and the interphase/interface region. One exception is the M2 at $\epsilon=0.15$, where the Λ_e and Λ_a are comparable to each other. For models M3 and M4 at strains $\epsilon=0.15$ and 0.3, with an increasing number of bridge chains and thus the capability to transport heat in the amorphous region, the interphase/interface resistances become relatively high, and the Λ_e starts to become much smaller than Λ_a (e.g., 28%–50%). All these reductions of effective thermal conductivity in the interlamellar region from that in the amorphous region reiterate the non-negligible roles of the thermal resistances at the interphase and interface regions.

C. Strain effect on the effective thermal conductivity

Figure 5 shows the dependence of the effective thermal conductivity of the entire interlamellar region on the external strain and interlamellar configuration (i.e., models in Table II). Figure 5(a) shows that applying external strains on the semicrystalline PE does not always increase the effective thermal conductivity, which contrasts with the strain effect on the amorphous PE. 15 This difference is due to the complexity of the interlamellar chain topology. Even for the PE models with the same crystallinity M1-M3, the strain effects appear differently. For M1, the Λ_e substantially decreases with increasing strains. One bridge chain and one loop chain connect the two crystalline stems at $\varepsilon = 0.15$ whereas only one bridge chain is left at $\varepsilon = 0.3$, as seen in Fig. 3(a). External strains probably help align the orientation of the only bridge chain but also destroy the connection made by the loop chain. Due to the limited heat transfer channels in the amorphous region, the thermal conductivity decreases with the increasing strain. A larger strain does not necessarily result in a higher thermal conductivity, which depends on the chain topologies and the number of channels in the interlamellar region. For M2, the Λ_e slightly decreases after applying strains, but the difference between $\varepsilon = 0.15$ and $\varepsilon = 0.3$ is very small. With increasing strains, the number of bridge chains still stays the same as two and these two chains do not significantly change their alignment and orientational order, as seen from Fig. 3(b). For M3, the Λ_e increases with strains. With three bridge chains and one tail chain always connecting the two crystalline stems, these four chains are stretched with a much better orientational order, as seen from Fig. 3(c). As shown in our previous work, a better orientation order in polymer chains assists their vibrational transport and thus enhances the thermal conductivity. The increasing trend of thermal conductivity with strains is more obvious in the model M4, with a much higher crystallinity and a larger number of bridge chains in the amorphous region (shown in Fig. 4). From the above analysis, the number of connecting chains between the two crystalline stems in the interlamellar region is important. The strain would likely increase the thermal conductivity if a large number of chains bridging in the interlamellar region, whereas the thermal conductivity could decrease or stay the same with increasing strains if fewer chains connect the two stems. In models M1 and M2, the external strain will not monotonously increase the thermal conductivity of the semicrystalline PEs, which

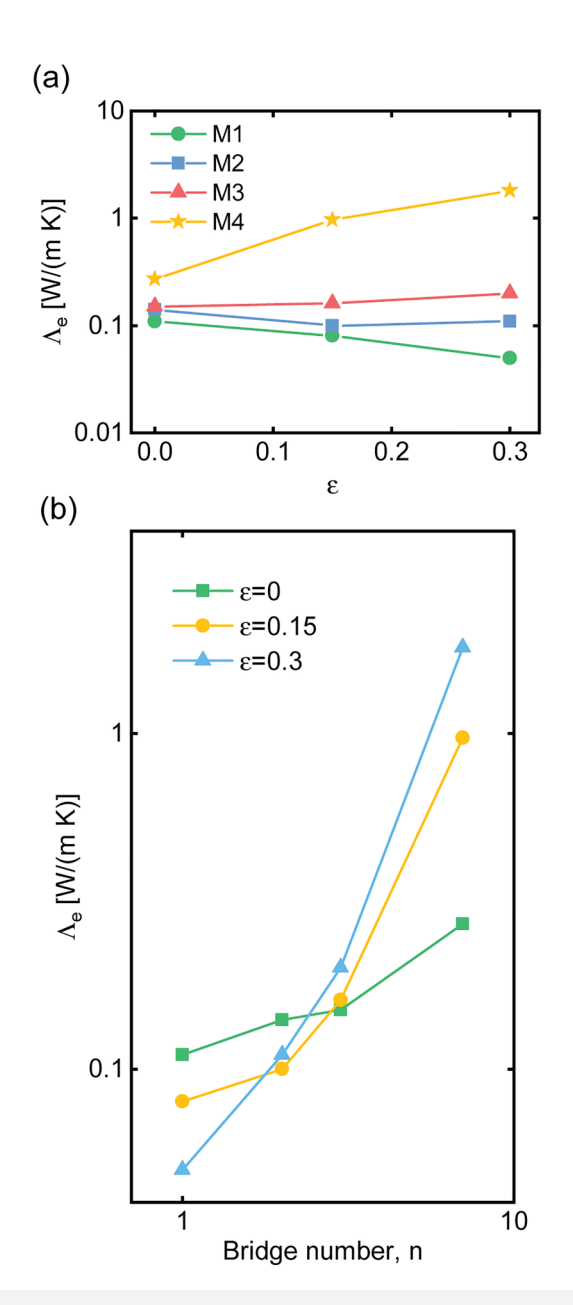


FIG. 5. The effective thermal conductivity of the interlamellar region for models M1–M4 as a function of (a) strain ε and (b) bridge number n.

is consistent with the recent experimental finding in stretched PE films. In the work by Xu *et al.*⁸ the thermal conductivity of stretched PE films with different draw ratios was measured. They also extracted the effective thermal conductivity in the amorphous region using reasonable analytical models. In Fig. 3 of their original publication, they have shown that at a moderate draw ratio (e.g., 20–60), the thermal conductivity for the entire film and the amorphous region does not vary substantially, with a fluctuation in the

range of 3–6 W/(m K) despite a triple variation in the draw ratio. This plateau region is beyond the initial increase in thermal conductivity with strains due to alignment of crystallites in the stretching direction, which is at a draw ratio less than 20. Our simulation does not start with stretching an isotropic semicrystalline PE; instead, our zero-strain model is a one-dimensional stacking semicrystalline structure, which mimics the experimental stretching at a moderate draw ratio where the crystallites are orientated in the stretching direction connected by the amorphous regions. Our simulation results match the overall trend with the recent experiment results at a moderate draw ratio and an intermediate crystallinity.

Figure 5(b) shows the dependence of effective thermal conductivity in the interlamellar region as a function of the bridge number at different strains. Overall, the effective thermal conductivity increases with the number of bridge chains, which extends the conclusion from our previous work on semicrystalline PE without strains²⁴ to these models with strains. Without strains, the bridge chains are not always aligned well with the heat flow direction, which are not in their most efficient state to transfer heat. In addition, the interactions with tail and loop chains weaken their ability to effectively transport heat. Therefore, the dependence of thermal conductivity on the bridge number is not significant in the unstretched models compared to the stretched ones. At strains $\varepsilon = 0.15$ and $\varepsilon = 0.3$, the interactions between bridge chains and tail/loop chains are reduced because most of the tail and loop chains shrink back to or stay in the interphase or interface region. The dependence of thermal conductivity on the bridge number is more substantial at these strains.

We can compare the effective thermal conductivity of the interlamellar region with the thermal conductivity of their bulk amorphous counterparts. As shown in our previous work, the thermal conductivity of bulk amorphous PE using the same force field is $0.12 \pm 0.02 \, \text{W/(m\,K)}.^{24}$ Except for model M2, the other models M1, M3, and M4 do not have the same thermal conductivity as the bulk amorphous PE, with and without strains. Our previous work²⁴ pointed out that the thermal conductivity of semicrystalline PEs without strains does not match that of the bulk amorphous counterparts, especially at high crystallinities. This work extends this conclusion to semicrystalline PEs with strains, which represent the models of stretched PE films and highly aligned PE fibers. Therefore, the interlamellar chain topologies are important to determine the thermal conductivity of semicrystalline polymers.

D. Vibrational energy transport in the interphase region

The above analysis on the thermal conductivity of semicrystal-line PE, the thermal resistances at different regions, and the strain effect focuses on the thermal conductivity and resistance only. To understand the energy transport in the interlamellar region from the vibrational mode perspective, we will analyze the mode contribution to heat flux in selected regions. The heat transfer mechanism in the amorphous region is relatively better understood (if not fully understood) in the literature compared to the other two regions, both with and without strains. Without strains, the thermal transport in the amorphous region is similar to that in the amorphous polymer. ^{15,48,49} With strains, the thermal transport in bridge chains is similar to that in single polymer chains. ^{16,50} It remains elusive

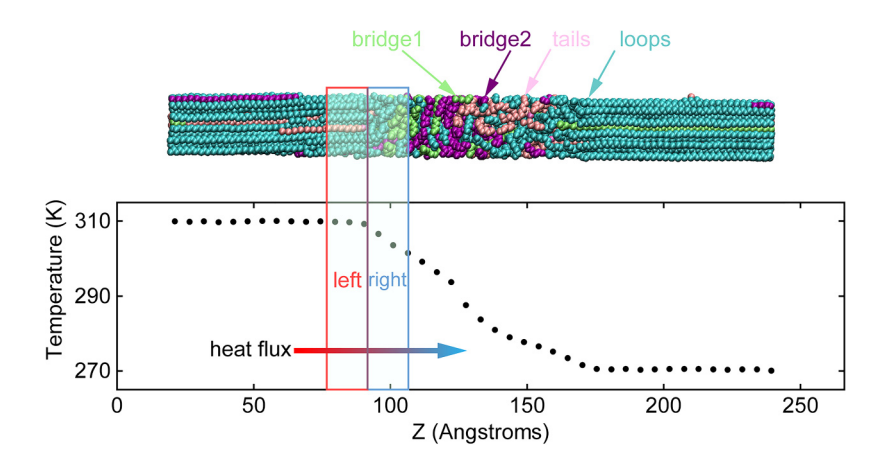


FIG. 6. Applying the FDDDM to the interphase region in model M2_0. The model M2 contains two bridge chains (bridge 1 and bridge 2), 10 tail chains, and 23 loop chains. Different from Fig. 3, the snapshot of this model is not repeated in the vertical direction for visualization. The interphase region is divided into left and right layers and the heat current flows from the left layer to the right layer. The temperature profile, i.e., the average temperature at each location Z, is also plotted.

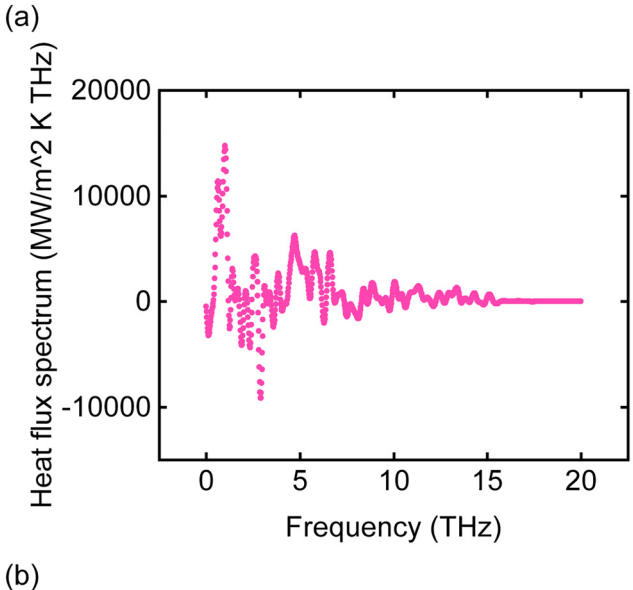
how the vibrational energy is transferred across the interphase and interface regions where the arrangement of atoms exhibits a transition from the crystalline order to amorphous disorder.

To understand the contribution to heat flux from vibrational modes, we conducted the analysis using the frequency domain direct decomposed method (FDDDM) to solve the heat flux spectrum across the crystalline-amorphous interphase region in the semi-crystalline PE, following the method described in Ref. 41. Figure 6 shows the concept of applying FDDDM to semi-crystalline models. A standard NEMD method is applied to establish a thermal gradient across the interlamellar region. We selected the interphase region, as marked, as the "control volume" in the FDDDM. For example, in our model M2_0, we selected the control volume at the central position z = 91.8 Å with a thickness of 30 Å, which contains 667 atoms. We then divided the control volume into two layers, left and right layers, and calculated the frequencydependent thermal conductance across an individual interface between the left and right layers following Eq. (4) in Ref. 41. In the model in Fig. 6, the temperature drop within the interphase control volume is ~ 10 K. Such a small temperature variation in the control volume limits the atomic displacement to be much smaller than the distance between atomic equilibrium positions but inevitably results in significant noise in the heat current spectrum. We applied a Gaussian filter to suppress the noise in the spectrum with an optimized cut-off frequency in the range of 0.1-0.5 THz. A larger cut-off frequency leads to a more accurate sampling but with more random noise, whereas a smaller cut-off frequency results in a smooth spectrum but with a potential distortion in the spectrum. In addition, we found that a statistically large number of atoms in the control volume (e.g., >600) is necessary to provide a statistically meaningful heat current spectrum with suppressed noise. In this work, we only applied the FDDDM analysis to the unstretched M2 model as a representative model, which has enough atoms in the interphase region and can maintain a reasonable temperature drop in the same model. After reaching the steady state in the NEMD simulation, the equilibrium positions of atoms were calculated by averaging the atomic trajectory for 1 ns. Then, the displacement of each atom was recorded for 50 ps. By calculating the heat flux between atoms in left and right layers following Ref. 41, we calculated the heat flux spectrum in the interphase region.

Figure 7(a) shows the heat flux spectrum in the interphase region of model M2_0. In general, vibrational modes with lower frequencies (<5 THz) carry more heat flux than high frequencies (10-15 THz). This trend is as expected because the low-frequency modes usually have higher thermal diffusivities on a per mode basis, especially for these modes involving atoms on the covalently bonded chains. Because of the complicated chain topologies in the interphase region, especially the loop chains, the heat transfer along the chain can be in the +z or -z directions, which results in positive or negative atomic heat fluxes in Fig. 7(a). This negative atomic heat flux does not violate the second law of thermodynamics or Fourier's law because accumulatively the heat current still flows from the high-temperature side to the low-temperature side. The loop chains and tail chains are covalently bonded, which result in negative heat fluxes with large magnitudes at low frequencies. Therefore, even though the magnitude of the heat flux contributed from lower-frequency vibrational modes is large, the negative heat flux in this region limits the net heat transfer and creates thermal resistances in this region.

We note here that the limited size of our simulation domain might suppress the contribution to the total heat flux from vibrational modes with long mean-free-paths or long modal spatial extent (an analogous concept for localized modes). The simulation-domain-induced size effect in the computed thermal conductivity and interfacial thermal resistance using the NEMD method is well known where vibrational modes with wavelengths or mean-free-paths much longer than the domain size are not supported in the simulation. Recently, we have published a computational work⁴⁹ on the size effect of the thermal conductivity in an amorphous polymer, which shows that the mean-free-path of propagating heat carriers can range from tens of nanometers to more than 100 nm, contributing 16%-36% of the total thermal conductivity. A recent experimental work⁵⁰ indicates that the vibrational modes with mean-free-paths more than 200 nm make a non-negligible contribution thermal to transport crystalline-amorphous interfaces even though there are substantial microstructural imperfections in the specimen.

We also note that previous simulation works demonstrated the importance of vibrational modes with high frequency (>5 THz) on the thermal transport in both crystalline and amorphous polymers. Vibrational modes with relatively high frequency or limited



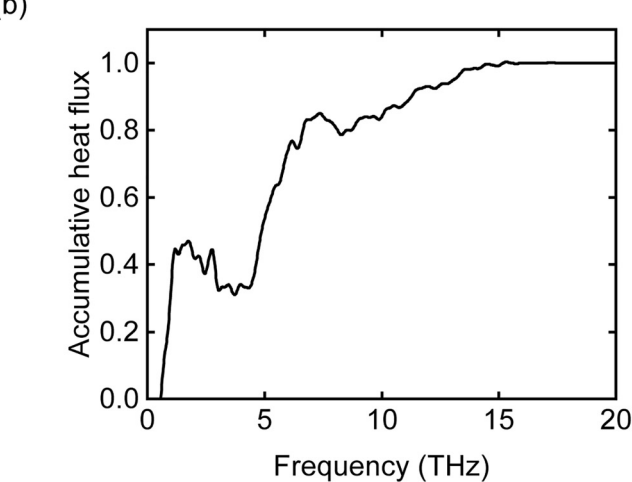


FIG. 7. Analysis of the heat flux spectrum using the FDDDM. (a) The heat flux spectrum as a function of frequency in the interphase region of model M2_0. (b) The normalized accumulative heat flux as a function of frequency in the interphase region of model M2_0.

modal spatial extent were not generally considered as significant contributors to the total thermal conductivity or interfacial thermal conductance in inorganic materials. However, first-principles calculations of the phonon transport in the PE chain and crystal by Wang *et al.*⁵¹ show that the contribution to the total thermal conductivity from modes with frequencies less than 5 THz is only less than 20%, with the major contribution from modes with frequencies in the range of 5–15 THz. Molecular dynamics simulation and normal mode analysis of thermal transport in amorphous polymers show that spatially localized modes with high frequencies (\gg 5 THz) and low modal spatial extent (\sim 1 nm) contribute >80% to the total thermal conductivity due to their large population.⁵²

Although the delocalized modes contribute more to thermal conductivity than these spatially localized modes on a per mode basis, their overall contribution is less than 20% in amorphous polymers.

Figure 7(b) shows the accumulative heat flux as a function of frequency. Although the interatomic heat fluxes at low frequencies have large magnitudes, they only accumulatively contribute ~40% of the total heat flux up to ~5 THz because of the negative heat fluxes with similar magnitudes. The vibrational modes with frequencies between 5 and 10 THz contribute ~50% heat flux and modes with frequencies above 10 THz carry the rest 10% energy across the interphase region. Even though it has been demonstrated that vibrational modes with middle to high frequencies can also contribute to heat transfer across other interfaces, such as Si/Ge interfaces, 45,53 the interphase region investigated in this work is unique because of the covalently bonded chains with topologies such as loop and tail. Our analysis shows that vibrational modes at intermediate and high frequencies can contribute more than these at low frequencies to the total heat flux in the interphase region of semicrystalline polymers. Even though the simulation size effects might exist, the effect of cancellation of positive and negative heat fluxes at low frequencies due to chains with topologies could still dominate.

Further investigations will be needed to validate this phenomenon and potentially extend this phenomenon to any interface or region with complex topology in the future. For example, to excite more delocalized modes within the simulation domain and examine their role, a thicker interphase region and a larger crystalline region would be helpful. A mode-level analysis is also useful to understand the contribution from different types of vibrational modes. For example, a few recent publications pointed out the importance of the interfacial modes for the interfacial thermal transport. From the normal mode analysis,⁵⁴ it is found that the interfacial modes at the crystal/amorphous interface can have the highest per mode contribution to the interfacial thermal conductance among all modes. Similarly, from the modal NEMD method, 45 it is found that the few atomic layers at the interface are dominated by interfacial modes, which contribute more than 50% to the total thermal conductance in a model Si/Ge system.

IV. SUMMARY AND OUTLOOK

In this work, we built four semicrystalline PE models with different crystallinities and chain topologies and analyzed their thermal transport properties with and without strains. We show that it is the interlamellar chain topologies that determine the dependence of thermal conductivity on strains. As expected, bridge chains that connect the two crystalline stems are the major contributor to the thermal transport in the amorphous region of semicrystalline PEs with strains. But if loop or tail chains can attach to the opposite side of the crystalline stem, they will function as if they were bridge chains, even if this connection is not via covalent bonds. Contrary to many previous models, the effective thermal conductivity in the interlamellar region of drawn semicrystalline PE is not the same as the bulk amorphous counterpart, with and without strains. By analyzing the thermal resistances at the interlamellar region of models with strains, we find that the thermal resistance of the interphase region and the interface between the interphase region and the amorphous region could be dominant

resistances, compared to the thermal resistance at the amorphous region (even with longitudinal voids), which was usually assumed to be the source of the largest resistance. We conducted the frequency domain analysis to obtain the heat flux spectrum across the crystalline-amorphous interphase region and found that the vibrational modes at intermediate and high frequencies can contribute more than these at relatively low frequencies to the total heat flux because of the complex interlamellar chain topologies. A modelevel vibrational analysis in the future will enable a more detailed explanation of this observation. In addition, a larger simulation domain and a much slower strain rate would potentially lead to a more diverse interlamellar chain topology and a more comprehensive structure-property relationship. Our work provides fundamental understandings of thermal transport in semicrystalline polymers with strains, which could assist the development of plastic heat sinks and thermal management in flexible electronics.

ACKNOWLEDGMENTS

The authors would like to thank Yanguang Zhou for helpful discussions and thank Gregory C. Rutledge and Raghavan Ranganathan for their help in building the semicrystalline PE model. Computational resources were provided by the High-Performance Computing Center at North Carolina State University and the Extreme Science and Engineering Discovery Environment (XSEDE) that is supported by the National Science Foundation (NSF) under Grant No. ACI-1548562. The authors acknowledge the financial support from the National Science Foundation under Award No. CBET 1943813. This work was also supported by the Faculty Research and Professional Development Fund from North Carolina State University.

AUTHOR DECLARATIONS

Conflicts of Interest

The authors do not have any conflict of interest to disclose.

DATA AVAILABILITY

The data that support the findings of this study are available from the corresponding author upon reasonable request.

REFERENCES

- ¹X. Wei, Z. Wang, Z. Tian, and T. Luo, J. Heat Transfer 143, 072101 (2021).
- ²A. L. Moore and L. Shi, Mater. Today 17, 163-174 (2014).
- ³H. Ma, B. Gao, M. Wang, Z. Yuan, J. Shen, J. Zhao, and Y. Feng, J. Mater. Sci. 56, 1064–1086 (2021).
- ⁴G. Li, R. Zhu, and Y. Yang, Nat. Photonics **6**, 153–161 (2012).
- ⁵J. Allen, Energy Rep. **6**, 217–224 (2020).
- ⁶A. R. J. Hussain, A. A. Alahyari, S. A. Eastman, C. Thibaud-Erkey, S. Johnston, and M. J. Sobkowicz, Appl. Therm. Eng. 113, 1118–1127 (2017).
- ⁷S. Shen, A. Henry, J. Tong, R. Zheng, and G. Chen, Nat. Nanotechnol. 5, 251–255 (2010).
- ⁸Y. Xu, D. Kraemer, B. Song, Z. Jiang, J. Zhou, J. Loomis, J. Wang, M. Li, H. Ghasemi, X. Huang, X. Li, and G. Chen, Nat. Commun. 10, 1771 (2019).
- ⁹Z. Zhong, M. C. Wingert, J. Strzalka, H.-H. Wang, T. Sun, J. Wang, R. Chen, and Z. Jiang, Nanoscale 6, 8283–8291 (2014).
 ¹⁰V. Singh, T. L. Bougher, A. Weathers, Y. Cai, K. Bi, M. T. Pettes,
- ¹⁰V. Singh, T. L. Bougher, A. Weathers, Y. Cai, K. Bi, M. T. Pettes, S. A. McMenamin, W. Lv, D. P. Resler, T. R. Gattuso, D. H. Altman, K. H. Sandhage, L. Shi, A. Henry, and B. A. Cola, Nat. Nanotechnol. 9, 384–390 (2014).

- ¹¹G.-H. Kim, D. Lee, A. Shanker, L. Shao, M. S. Kwon, D. Gidley, J. Kim, and K. P. Pipe, Nat. Mater. 14, 295–300 (2015).
- 12Y. Wu, X. Zhang, A. Negi, J. He, G. Hu, S. Tian, and J. Liu, Polymers 12, 426 (2020).
- ¹³A. Shanker, C. Li, G.-H. Kim, D. Gidley, K. P. Pipe, and J. Kim, Sci. Adv. 3, e1700342 (2017).
- ¹⁴Y. Xu, X. Wang, J. Zhou, B. Song, Z. Jiang, M. Y. Lee Elizabeth, S. Huberman, K. Gleason Karen, and G. Chen, Sci. Adv. 4, eaar3031 (2018).
- ¹⁵J. Liu and R. Yang, Phys. Rev. B **81**, 174122 (2010).
- ¹⁶J. Liu and R. Yang, Phys. Rev. B **86**, 104307 (2012).
- 17 J. He, K. Kim, Y. Wang, and J. Liu, Appl. Phys. Lett. 112, 051907 (2018).
- ¹⁸X. Wang, V. Ho, R. A. Segalman, and D. G. Cahill, Macromolecules 46, 4937–4943 (2013).
- 19 B. Zhu, J. Liu, T. Wang, M. Han, S. Valloppilly, S. Xu, and X. Wang, ACS Omega 2, 3931–3944 (2017).
- ²⁰R. Shrestha, P. Li, B. Chatterjee, T. Zheng, X. Wu, Z. Liu, T. Luo, S. Choi, K. Hippalgaonkar, M. P. de Boer, and S. Shen, Nat. Commun. 9, 1664 (2018).
- ²¹C. L. Choy, Polymer 18, 984–1004 (1977).
- ²²P. J. in 't Veld and G. C. Rutledge, Macromolecules 36, 7358-7365 (2003).
- ²³J. Hennig, J. Polym. Sci. Part C: Polym. Symp. **16**, 2751–2761 (1967).
- ²⁴T. Lu, K. Kim, X. Li, J. Zhou, G. Chen, and J. Liu, J. Appl. Phys. **123**, 015107 (2018).
- ²⁵J. Liu, M. Alhashme, and R. Yang, Carbon 50, 1063–1070 (2012).
- ²⁶Y. Wang, J. Liu, J. Zhou, and R. Yang, J. Phys. Chem. C 117, 24716–24725 (2013).
- ²⁷F. Sun, T. Zhang, M. M. Jobbins, Z. Guo, X. Zhang, Z. Zheng, D. Tang, S. Ptasinska, and T. Luo, Adv. Mater. 26, 6093–6099 (2014).
- ²⁸M. Takayanagi, K. Imada, and T. Kajiyama, J. Polym. Sci. Part C: Polym. Symp. 15, 263–281 (1967).
- ²⁹J. C. H. Affdl and J. L. Kardos, Polym. Eng. Sci. **16**, 344–352 (1976).
- ³⁰H. L. Cox, British J. Appl. Phys. **3**, 72–79 (1952).
- 31 A. Peterlin, Colloid Polym. Sci. 265, 357–382 (1987).
- 32 A. Keller, Rep. Prog. Phys. 31, 623–704 (1968).
- ³³A. Peterlin, J. Mater. Sci. 6, 490–508 (1971).
- ³⁴J. F. Twisleton, J. W. White, and P. A. Reynolds, Polymer **23**, 578–588 (1982).
- 35 S. Lee and G. C. Rutledge, Macromolecules 44, 3096–3108 (2011).
- ³⁶J. M. Kim, R. Locker, and G. C. Rutledge, Macromolecules 47, 2515–2528 (2014).
 ³⁷I.-C. Yeh, J. W. Andzelm, and G. C. Rutledge, Macromolecules 48, 4228–4239
- ³⁸I.-C. Yeh, J. L. Lenhart, G. C. Rutledge, and J. W. Andzelm, Macromolecules 50, 1700–1712 (2017).
- ³⁹R. Ranganathan, V. Kumar, A. L. Brayton, M. Kröger, and G. C. Rutledge, Macromolecules 53, 4605–4617 (2020).
- 40 Y. Lu, J. Liu, X. Xie, and D. G. Cahill, ACS Macro Lett. 5, 646-650 (2016).
- 41 Y. Zhou and M. Hu, Phys. Rev. B **92**, 195205 (2015).
- ⁴²G. T. Dee, T. Ougizawa, and D. J. Walsh, Polymer **33**, 3462–3469 (1992).
- 43 S. Plimpton, J. Comput. Phys. 117, 1–19 (1995).
- ⁴⁴L. Yang, B. Latour, and A. J. Minnich, Phys. Rev. B **97**, 205306 (2018).
- 45 T. Feng, Y. Zhong, J. Shi, and X. Ruan, Phys. Rev. B 99, 045301 (2019).
- ⁴⁶X. Duan, Z. Li, J. Liu, G. Chen, and X. Li, J. Appl. Phys. **125**, 164303 (2019).
- ⁴⁷J. He and J. Liu, J. Appl. Phys. **129**, 215102 (2021).
- ⁴⁸T. Zhang and T. Luo, J. Phys. Chem. B **120**, 803–812 (2016).
- ⁴⁹T. Feng, J. He, A. Rai, D. Hun, J. Liu, and S. S. Shrestha, Phys. Rev. Appl. 14, 044023 (2020).
- ⁵⁰A. B. Robbins, S. X. Drakopoulos, I. Martin-Fabiani, S. Ronca, and A. J. Minnich, Proc. Natl. Acad. Sci. U.S.A. 116, 017163–17168 (2019).
- 51X. Wang, M. Kaviany, and B. Huang, Nanoscale 9, 018022–18031 (2017).
- 52B. Li, F. DeAngelis, G. Chen, and A. Henry "Normal mode analysis of the thermal conductivity in amorphous polymers: The importance of localized modes," Nature (published online).
- 53K. Gordiz and A. Henry, Sci. Rep. 6, 023139 (2016).
- ⁵⁴K. Gordiz and A. Henry, J. Appl. Phys. **121**, 025102 (2017).